**Showcasing research from Doctor Gyujin Song's group, Korea Institute of Energy Research, Ulsan, Republic of Korea.**

Dual-fibrous PTFE structure enabling uniform and thick dry electrodes for high-energy-density and long-lasting batteries

A novel dual-fibrous PTFE binder structure is introduced through a stepwise fabrication to advance dry-processed battery electrodes. Our approach improves structural, electrochemical homogeneity and mechanical durability for high-energy-density and stable lithium-ion batteries.

Image reproduced by permission of Gyujin Song from *Energy Environ. Sci.*, 2025, **18**, 8446.

As featured in:

Energy & Environmental Science
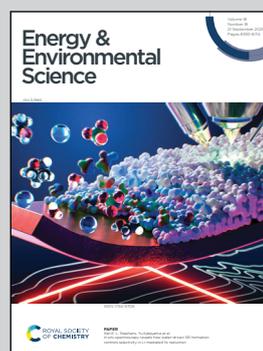
See Tae-Hee Kim, Gyujin Song *et al.*, *Energy Environ. Sci.*, 2025, **18**, 8446.

PAPER

Check for updates

Dual-fibrous PTFE structure enabling uniform and thick dry electrodes for high-energy-density and long-lasting batteries

Kwon-Hyung Lee, [ID] †[ac] Hyeongseok Shim, [ID] †[ad] Sang Hyun Lee,[a]
Hyeong-Jong Kim,[e] Chanhyun Park, [ID][e] Jingyu Choi,[e] Seok-Ju Lee,[f]
Young-Kuk Hong,[f] Jihong Lyu,[g] Jin Chul Kim, [ID][g] Sijeong Park,[ae]
Hyungyeon Cha,[a] Wooyoung Jin,[a] Jinsoo Kim,[h] Sinho Choi,[a] Sang-Young Lee, [ID][f]
Sung-Kyun Jung, [ID][ijkl] Michael De Volder, [ID][c] Tae-Hee Kim*[b] and Gyujin Song [ID] *[a]

Dry-processed electrodes based on poly(tetrafluoroethylene) (PTFE) binder have emerged as a promising technology for sustainable, low-cost and high-areal-capacity electrode manufacturing. However, understanding its fibrillation behaviour becomes a key engineering factor to achieve mechanically robust electrodes with high electrochemical performance. Herein, we present a dual-fibrous dry electrode (DDE) fabricated *via* a multi-step grinding and kneading process. Compared to conventional single-type fibrous structures, the proposed DDE exhibits a more uniform material distribution, enabling better electronic conductivity and reaction homogeneity, which in turn results in better cycling stability. Additionally, the PTFE rope in the DDE demonstrates excellent mechanical integrity and edge uniformity—critical attributes for roll-to-roll manufacturing. Overall, our DDE achieves a high areal capacity of 10.1 mAh cm^{-2} with stable cycle retention. Furthermore, a 1.2 Ah-class stacked pouch full cell incorporating the DDE delivers a high energy density of 349 Wh kg$_{cell}^{-1}$/800 Wh L$_{cell}^{-1}$ when paired with a lithium metal anode, and exhibits 80.2% capacity retention after 600 cycles when paired with a graphite anode, demonstrating superior performance compared to previously reported dry electrodes.

Broader context

The global shift toward the electrification have accelerated the development of advanced higher energy density batteries. However, the conventional slurry-based battery electrodes face challenges, linked to high energy consumption and to uneven carbon–binder domain (CBD) distribution, increasing the interest in dry-processed electrode manufacturing. Poly(tetrafluoroethylene) (PTFE)-based dry electrodes have garnered attention for enabling thick and dense electrode structure, however, their poor homogeneity and poor mechanical properties hinder further practical application. This work proposes a dual-fibrous PTFE binder structure to achieve homogeneous and sturdy dry electrodes by addressing key engineering factors in the electrode fabrication process. Compared to conventional fibrous structures, the dual-fibrous dry electrode (DDE) shows enhanced mechanical integrity and material uniformity, delivering a high areal capacity of 10.1 mAh cm^{-2}. Furthermore, a 1.2 Ah-class pouch cell incorporating the DDE achieved a high energy density of 349 Wh kg^{-1} when paired with a lithium metal anode, and demonstrated stable cycling performance, retaining 80.2% of its initial capacity after 600 cycles with a graphite anode. We envision that the dual-fibrous structure presented here can be widely adopted in practical dry electrode manufacturing as a versatile platform technology to enable high-energy-density batteries.

[a] Ulsan Advanced Energy Technology R&D Center, Korea Institute of Energy Research (KIER), Ulsan 44776, Republic of Korea. E-mail: gyujin.song@kier.re.kr

[b] School of Chemical Engineering, University of Ulsan, Ulsan 44610, Republic of Korea. E-mail: kimtaehee@ulsan.ac.kr

[c] Department of Engineering, University of Cambridge, Cambridge, CB3 0FS, UK

[d] School of Materials Science and Engineering, Kyungpook National University, Daegu, 41566, Republic of Korea

[e] School of Energy and Chemical Engineering, Ulsan National Institute of Science and Technology (UNIST), Ulsan 44919, Republic of Korea

[f] Department of Chemical and Biomolecular Engineering, Yonsei University, Seoul 03722, Republic of Korea

[g] Department of Specialty Chemicals, Division of Specialty and Bio-based Chemicals Technology, Korea Research Institute of Chemical Technology (KRICT), Ulsan 44412, Republic of Korea

[h] Department of Energy Science and Engineering, Daegu Gyeongbuk Institute of Science and Technology (DGIST), Daegu 42988, Republic of Korea

[i] Research Institute of Advanced Materials (RIAM), Seoul National University (SNU), Seoul 08826, Republic of Korea

[j] School of Transdisciplinary Innovations, Seoul National University (SNU), Seoul 08826, Republic of Korea

[k] Department of Materials Science and Engineering, Seoul National University (SNU), Seoul 08826, Republic of Korea

[l] Institute for Rechargeable Battey Innovations Research, Seoul National University (SNU), Seoul 08826, Republic of Korea

† These authors contributed equally to this work.

8446 | *Energy Environ. Sci.*, 2025, **18**, 8446–8461

This journal is © The Royal Society of Chemistry 2025

Introduction

The increasing demand for electric vehicles, grid-scale energy storage systems, and next-generation portable electronics has driven rapid advancements in fast-charging, high-energy-density, and cost-effective lithium-ion batteries (LIBs).[1–3] In parallel, the global transition toward net-zero emissions has intensified focus on the environmental impact as well as capital and operational expenditures associated with battery manufacturing. Among the various stages of production—from material preparation to cell assembly—the electrode fabrication process, particularly the coating and drying steps, has been identified as one of the most cost- and energy-intensive processes, significantly influencing both manufacturing costs and environmental sustainability.[4–7] Conventional electrodes are produced *via* a wet-coating process in which electrode slurries are dispersed in processing solvents, necessitating a subsequent drying step, thereby increasing both energy consumption and overall cost.[7–9] Furthermore, solvent-drying can induce non-uniform compositional gradients along the electrode thickness direction, primarily due to carbon–binder domain (CBD) migration. During the drying process, CBD migration leads to binder accumulation near the electrode surface, resulting in poor adhesion and electrochemical performance, particularly in thick electrodes. This unintended behaviour undermines electrochemical and mechanical performance and creates environmental concerns.[10–13]

Dry coating of battery electrodes (DBEs) is a promising alternative to conventional electrode manufacturing, as they eliminate both the need for toxic solvents and the energy-intensive drying step.[14,15] Recently, the battery industry has focused on poly(tetrafluoroethylene) (PTFE) as a binder for DBEs due to its unique shear-induced fibrillation behaviour, which enables uniform electrode thickness, compatibility with roll-to-roll manufacturing, mechanical flexibility, and thermal stability.[16,17] The typical PTFE-based DBE manufacturing process involves three primary steps: (1) powder preparation, including mixing and kneading to induce PTFE fibrillation; (2) sheet formation to produce an electrode dough; (3) roll pressing to create free-standing electrode films and lamination onto current collector. Due to the absence of a dispersing solvent, achieving microscale homogeneous distribution of electrode components remains a critical challenge. Fine control of structure-forming factors, such as high-torque shear and prolonged mixing and/or kneading, is necessary to ensure a uniform material distribution within the DBE. However, excessively high-torque processing can degrade the PTFE fibrous network, resulting in poor mechanical properties.[17,18] In roll-to-roll manufacturing, such degradation may lead to structural failure, disrupting the entire fabrication line. Therefore, it is essential to secure a robust PTFE fibrous structure with a homogeneous microscale distribution of components through carefully optimised powder preparation procedures.

The fundamental concept of PTFE fibrillation was studied by Kanazawa *et al.*, who demonstrated that folded lamellae fiber composed of PTFE particles can be extended under shear force.[19] Building on this concept, various studies on PTFE-based DBE have reported using different cathode active materials, including LiNi$_{0.6}$Co$_{0.2}$Mn$_{0.2}$O$_2$ (NCM622), LiNi$_{0.8}$Co$_{0.15}$Al$_{0.05}$O$_2$ (NCA), LiNi$_{0.5}$Mn$_{1.5}$O$_4$ (LNMO), and LiFePO$_4$ (LFP).[17,20–22] Despite these advancements, a comprehensive understanding of the fibrous binder structure at the electrode level remains elusive. Paik *et al.* investigated the thermomechanical properties of PTFE binders and their influence on the electrochemical performance of DBEs, providing valuable insights into PTFE fibrillation behaviour and associated electrochemical characteristics.[23] More recently, several studies have revisited PTFE fibrillation mechanisms in the pursuit of advanced DBE architectures,[24,25] however, a clear understanding of the optimal binder structure and its effects on the physical, mechanical, and electrochemical properties is still lacking.

Here, we present a dual-fibrous dry electrode (DDE), engineered to simultaneously improve electrode homogeneity and mechanical integrity. The DDE was developed through a stepwise fibrillation approach involving a multi-step grinding and kneading process, yielding two distinct types of fibrillated PTFE: yarn-like thin fibres (PTFE fibre) and rope-like thick fibres (PTFE rope). The stepwise kneading-grinding-kneading procedure enabled homogeneous microscale distribution of the electrode components, in which the second kneading step produced the PTFE rope composed of multiple inter-twined PTFE fibres. Especially, the thick PTFE ropes bind the electrode particles together in conjunction with the PTFE fibres, resulting in an improved mechanical integrity and smoother edge roughness. These are all critical attributes for roll-to-roll manufacturing and subsequent cell assembly at an industrial scale.

The DDE manufactured by the above multi-step grinding and kneading processes, enabled the fabrication of a high-areal-capacity single-crystal LiNi$_{0.8}$Co$_{0.1}$Mn$_{0.1}$O$_2$ (sc-NCM811) cathode with exceptionally high areal capacities (>10 mAh cm^{-2} and > 50 mg cm^{-2}), while at the same time achieving excellent electrochemical stability. The enhanced electrochemical performance of the DDE was demonstrated in 1.2 Ah-class pouch cells, where lithium metal (Li)||DDE and graphite (Gr)||DDE configurations achieved high energy densities of 349 Wh kg^{-1}/ 800 Wh L^{-1} and 291 Wh kg^{-1}/685 Wh L^{-1}, respectively. Moreover, the Gr||DDE pouch cell demonstrated stable capacity retention of 80.2% after 600 cycles which surpasses the previously reported dry electrodes. In addition, the entire fabrication process of the DDE can be easily adapted to commercial production line, emphasising its practical advantages for large-scale battery production. These properties highlight the DDE's advantages in both efficient electrode/cell manufacturing *via* roll-to-roll processes and long-term electrochemical and structural stability under practical conditions.

Results and discussion

Stepwise fabrication of high-areal-capacity electrodes based on dual-fibrous PTFE structure

Powder preparation steps significantly influence the fibrous structure of PTFE and the resulting physical and electrochemical properties of dry electrodes due to the absence of a processing solvent; thus, careful engineering of the powder preparation is
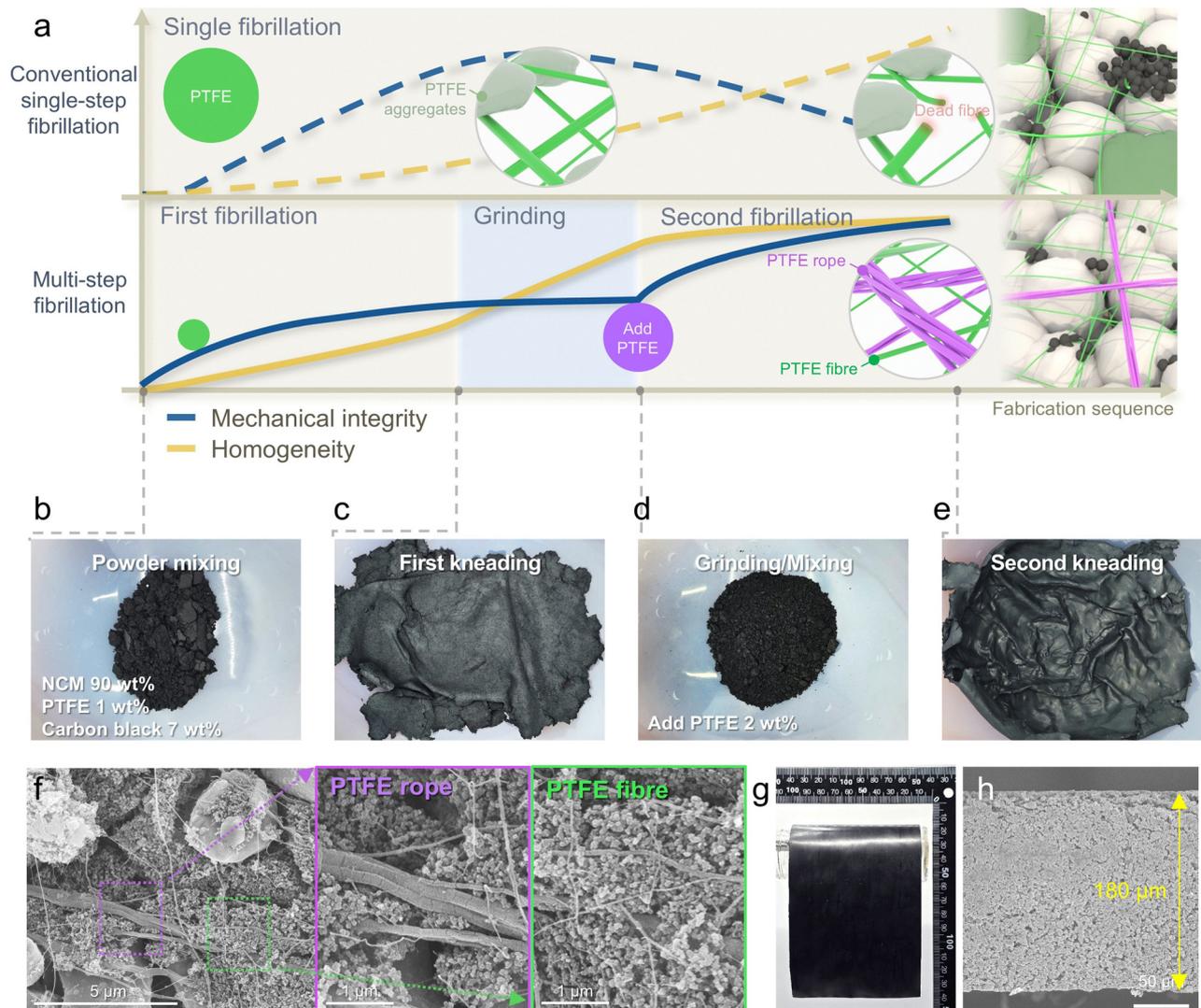
This journal is © The Royal Society of Chemistry 2025

Energy Environ. Sci., 2025, **18**, 8446–8461 | **8447**

Fig. 1 Structure-forming mechanism of dual-type PTFE fibrous structure. (a) Schematic illustration of comparison of the fabrication procedure between multi-step grinding/kneading process for DDE and conventional single-step fibrillation for SDE. Inset images show schematic representation of PTFE fibrous structure. Right images show schematic representation of SDE and DDE. (b)–(e) Photographs for DDE according to fabrication steps: (b) powder mixing of sc-NCM811 and CB with 1 wt% PTFE, (c) first kneading step, (d) grinding/mixing after the addition of 2 wt% PTFE, and (e) second kneading step. (f) SEM images showing PTFE rope and PTFE fibre in the DDE. (g) Photograph and (h) cross-sectional SEM image of as-roll pressed DDE.

essential to optimise PTFE fibrous morphology. Fig. 1(a) schematically illustrates the overall multi-step fibrillation process in comparison to conventional single-step fibrillation, along with the estimated electrode properties. The detailed fabrication procedure is described in Fig. S1a. Initially, sc-NCM811 and CB were mixed with 1 wt% PTFE (one-third of the final binder content) to lower the PTFE/CB ratio. The CB facilitates fibrillation of PTFE by anchoring to it and enhancing the transfer of shear force.[23,26,27] The surface of CB physically interlocks with the surface lamella fibres of the PTFE, establishing a strong anchoring point. Throughout the kneading process, the CB particles move away from each other, leading to the elongation of PTFE fibrils, which can be extended significantly under continued shear.[23,24] The relatively low PTFE/CB ratio (1/7, w/w) facilitated effective fibrillation by increasing the anchor point

between PTFE and CB, preventing the formation of tangle-shaped PTFE aggregates, which are often a problem in conventional single step fibrillation processes (Fig. 1(b)). In contrast, sc-NCM811 alone failed to induce sufficient PTFE fibrillation, highlighting the significant role of the CB in facilitating the fibrillation process (Fig. S1b). During the first kneading step, the applied shear force fibrillated the PTFE and formed an electrode "dough" (Fig. 1(c) and Fig. S1c).[28] This dough was then ground to break down large electrode granules, further enhancing microscale homogeneity, followed by the addition of 2 wt% PTFE binder and a subsequent mixing process, as shown in Fig. 1(d) and Fig. S1d. A second kneading step was performed to fabricate a PTFE rope, which is composed of multiple intertwined PTFE fibres. During this step, the initially fibrillated PTFE (1 wt%) maintained a thin fibrous morphology, while the

8448 | *Energy Environ. Sci.*, 2025, **18**, 8446–8461

This journal is © The Royal Society of Chemistry 2025

subsequently added PTFE (2 wt%) experienced relatively less shear force, resulting in the formation of PTFE rope composed of multiple inter-twined PTFE fibres, without noticeable fibre cleavage (Fig. 1(e) and (f)). To quantitively analyse the PTFE fibres and PTFE ropes, their diameter, length, and number of inter-twined fibres were monitored using image analysis (Fig. S2). The PTFE fibres exhibited average diameter and length of 48 nm and 1.3 μm, respectively. In contrast, PTFE rope showed much larger average diameter and extended length of 248 nm and 6.7 μm, respectively, along with 2–5 inter-twined fibres per rope. Such thick and elongated PTFE ropes in the DDE are advantageous for enhancing tensile strength and promoting entanglement between the ropes. In contrast, conventional single-step PTFE fibrillation (Fig. S1a) fails to form a uniform binder structure due to hinderance of shear forces transfer resulting in inconsistent binder coverage. A high PTFE/CB ratio of 3/7 (w/w) inhibits effective fibrillation due to insufficient physical contact between PTFE and CB, leading to the formation of tangled PTFE aggregates and only partial fibrous PTFE (Fig. S1e). Although identical grinding and second kneading steps were additionally applied as a control experiment (Fig. S1f and g), the uneven fibrillation of PTFE and resulting aggregates failed to undergo further fibrillation. These aggregates hinder effective shear force transfer, leading to localised over-kneading and excessive fibre fragmentation, which generate "dead fibres" (Fig. S1g). As an additional control sample, we extended the first kneading time without grinding step; however, this modification still failed to resolve the issue—electrodes with a high PTFE/CB ratio did not provide a uniform fibrous structure (Fig. S1h). To further investigate the effect of the PTFE/CB ratio, electrode powders with a wide range of compositions were analysed (Fig. S3a). At high PTFE/CB weight ratios (e.g., 3/1 and 9.5/0.5), large PTFE aggregates formed due to insufficient PTFE–CB contact. These aggregates also disrupted the electron transport network by introducing non-uniform component distribution, resulting in reduced electrical conductivity (Fig. S3b and c). Conversely, extremely low PTFE/CB ratios (e.g., 0.5/9.5) resulted in brittle structure that fracture. Based on these findings, a final weight composition of 3 wt% PTFE and 7 wt% CB was selected to balance electrical conductivity and mechanical properties. Scanning electron microscopy (SEM) images confirmed the formation of a well-developed, entangled dual-fibrous PTFE binder in the DDE, enabling an electrically conductive and robust electrode structure (Fig. S4a), whereas conventional single-fibrous dry electrode (SDE) exhibited only a partial fibrous network with tangled PTFE aggregates, leading to poor structural integration and localised contact loss within the electrode (Fig. S4b). These results highlight the uniqueness of the dual-fibrous structure and emphasize the importance of protocol engineering as a key structure-forming factor in achieving electrochemically and mechanically advanced dry electrode architectures.

Following the multi-step fibrillation, film formation, and roll pressing, the DDE exhibited smooth edges and a uniform electrode surface without noticeable defects (Fig. 1(g)). SEM images confirmed a uniform distribution of electrode components in the vertical direction, with an electrode thickness of 180 μm (Fig. 1(h)). Although roll pressing sometimes induced minor surface wrinkles—commonly referred to as "chattering" (Fig. S5a)—these were eliminated after lamination onto the current collector (Fig. S5b). In contrast, the SDE showed dark surface spots, indicating non-uniform distribution of components within the electrode (Fig. S5c).

Exploring the homogeneity of DDE through macro/micro-structural analyses

To gain a deeper understanding of electrode homogeneity, macro- and micro-scale analyses were conducted. As previously discussed in relation to the morphological structure shown in Fig. S4, the SDE exhibited randomly uncontacted regions that led to large voids, despite undergoing roll pressing intended to densify the porous structure. Mercury porosimetry measurements revealed a non-uniform pore size distribution in the SDE, characterized by a high fraction of pores exceeding 100 nm (Fig. 2(a)). This is primarily attributed to uncontrolled contact loss resulting from localised granule and particle agglomeration (Fig. S4b). This difference of pore structure was further confirmed using cross-sectional SEM and energy-dispersive X-ray spectroscopy (EDS) elemental mapping, in which the SDE showed irregular large voids and a heterogeneous morphological structure due to aggregated PTFE–CB clusters (Fig. S6a). In contrast, the DDE exhibited more uniform structure without irregular voids (Fig. S6b). The difference in conductive carbon distribution directly impacted the electronic conductivity of the electrodes: the DDE demonstrated a volumetric resistance of 1.29 Ω cm, which is approximately 1.4 times lower than that of the SDE (1.78 Ω cm), as shown in Fig. 2(b). These results emphasise the significance of electrode homogeneity for a well-connected electron conduction network.

In general, sc-NCM811 rarely exhibits crack formation during roll pressing due to its single-crystalline structure.[27] As a result, sc-NCM811 electrodes typically display relatively high surface roughness and a matte texture. In this regard, the surface roughness of the SDE and DDE was obtained to further verify the uniformity of active materials in the electrode. The SDE displayed coarse deviations and an inhomogeneous distribution of active materials at the surface (Fig. 2(c)). In contrast, the DDE exhibited smooth surface roughness and a relatively homogeneous distribution across the electrode (Fig. 2(d)). Furthermore, SEM and EDS elemental mapping of the electrode surface revealed clear differences in material distribution. The inferior fibrillation behaviour of the SDE resulted in a lopsided distribution of nickel (Ni) and carbon (C) atoms (Fig. 2(e)). This gradient may induce uneven electrochemical reactions of particles and selective particle degradation during prolonged electrochemical cycling.[28,29] In contrast, the DDE exhibited a uniform distribution throughout the electrode (Fig. 2(f)), underscoring the importance of the dual-fibrous structure of the PTFE binder in promoting electrode homogeneity.

To further investigate the electrode structure, advanced three-dimensional (3D) microstructural analysis was conducted using X-ray micro-computed tomography (micro-CT) to evaluate the uniformity of the DDE at both macroscopic and

This journal is © The Royal Society of Chemistry 2025

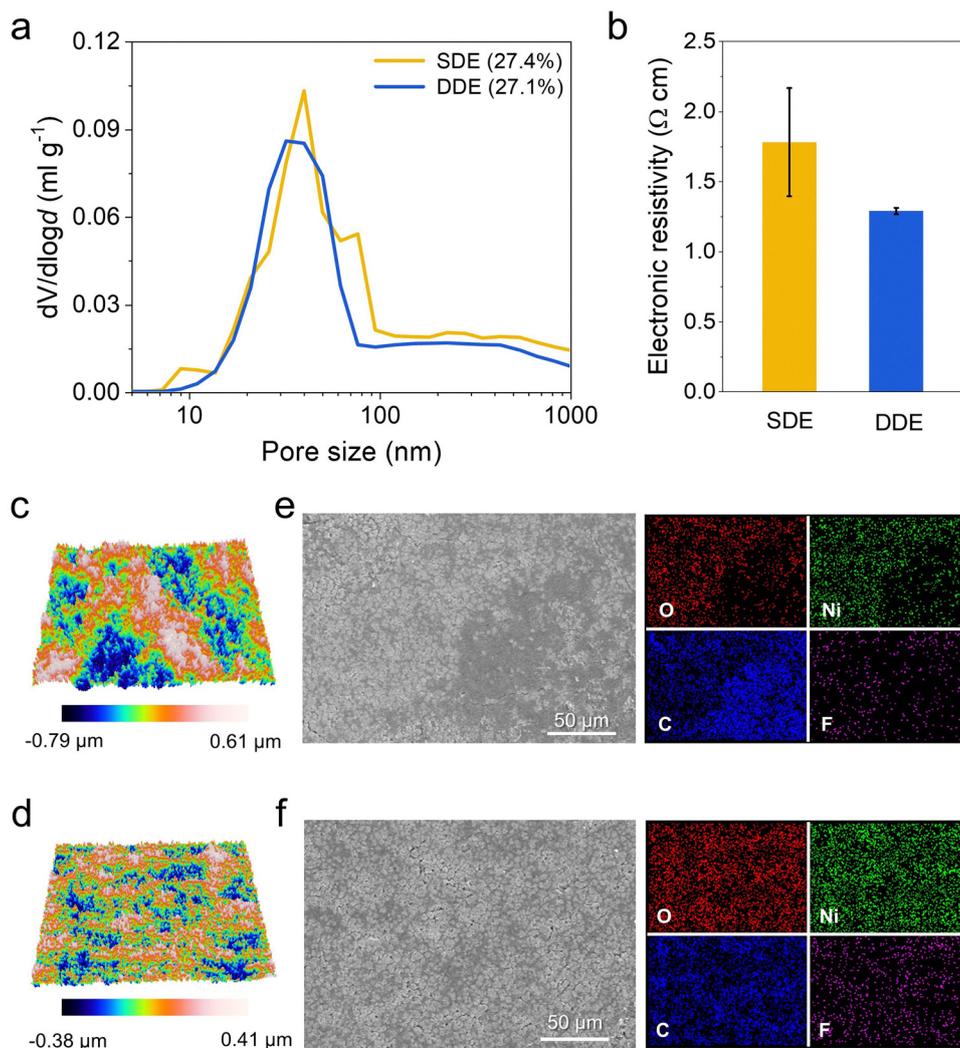*Energy Environ. Sci.*, 2025, **18**, 8446–8461 | **8449**

Fig. 2 Physical characterization for electrode homogeneity (a) Pore size distribution by mercury-intrusion porosimetry and (b) volumetric electronic resistivity of SDE and DDE. Surface roughness images showing electrode uniformity of (c) SDE and (d) DDE (338 μm × 283 μm). Top-view SEM images and corresponding EDS elemental mapping images of of (e) SDE and (f) DDE.

localised microscopic levels. As shown in the 3D reconstructed tomographic image, the SDE exhibited locally concentrated NCM-rich phases resulting from poor material homogeneity (Fig. 3(a)). Discrete pore–CB–PTFE domains may hinder efficient charge transport to the surrounding NCM particles, which could lead to localised variations in the state of charge and non-uniform electrochemical degradation during cycling. Additionally, the solid volume fraction of sc-NCM811 particles along the vertical axis was quantified through further image processing of the micro-CT data to comprehensively assess electrode homogeneity. The solid volume fraction represents the local density distribution of sc-NCM811, with a value of 1 indicating NCM-rich regions and 0 corresponding to pore/CB/ PTFE-rich regions. As shown in Fig. 3(b), the SDE exhibited an irregular distribution of solid volume fraction, with localised concentrations of NCM811 caused by the aggregation of PTFE–CB clusters.

In contrast, the DDE showed well-distributed sc-NCM811 domains embedded within a continuous and uniform pore–CB–PTFE network (Fig. 3(c)) and the corresponding solid volume fraction (Fig. 3(d)). These structural analyses underscore the beneficial role of the dual-fibrous structure in enhancing both electron transport pathways and structural integrity, thereby influencing overall electrochemical performance.

To evaluate the impact of electrode homogeneity on electrochemical performance, localised electrochemical impedance spectroscopy (LEIS), derived from scanning electrochemical microscopy (SECM), was employed to map the localised charge transfer resistance ($R_{l,ct}$) of the electrode, thereby verifying the correlation between structural uniformity and electrochemical reactivity. The low electrical conductivity and inhomogeneity of the SDE led to sluggish electrochemical kinetics and spatial variation in $R_{l,ct}$ values, indicating non-uniform charge transfer
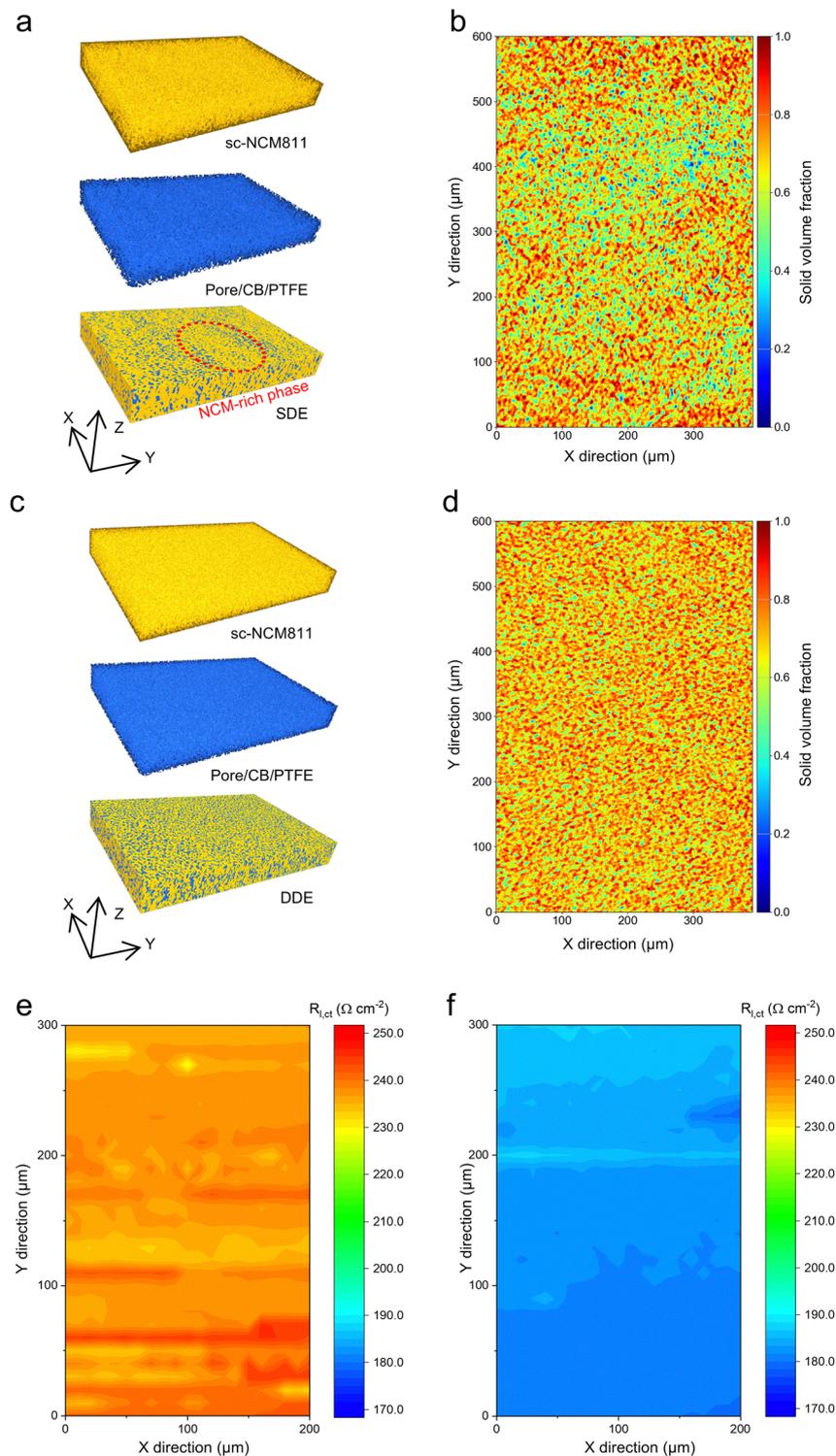
8450 | Energy Environ. Sci., 2025, 18, 8446–8461

This journal is © The Royal Society of Chemistry 2025

Fig. 3 Micro-structural analyses of thick dry electrode. (a) 3D reconstructed electrode images of the SDE measured by micro-CT, and (b) its corresponding volume fraction mapping image. (c) 3D reconstructed electrode images of the DDE, and (d) its corresponding volume fraction mapping image. Localized charge transfer resistance ($R_{l,ct}$) at 50% SOC of (e) SDE and (f) DDE measured by LEIS analysis.

within the electrode (Fig. 3(e)). In contrast, the DDE exhibited lower and more uniform $R_{l,ct}$ values compared to the SDE (Fig. 3(f)), enabling efficient electrochemical kinetics and promoting uniform charge transport throughout the electrode.

These localised, micro-scale electrochemical observations clearly demonstrate the critical role of structural uniformity in thick, dry electrodes to achieve good electronic conductivity and homogeneous reactivity.

Effect of PTFE rope on mechanical binding

During roll-to-roll manufacturing, dry-coated electrodes should have sufficient mechanical yield strength to withstand cracking and flaking and the starting material powder should have suitable flowability for consistent feeding.[30] In this context, the mechanical characteristics of the dry electrode were evaluated at the electrode level with respect to roll-to-roll processing. During roll pressing, the electrode edges are typically prone to damage due to uneven film elongation in both the machine direction and transverse direction. Given that the electrode width must be precisely tailored to the cell form factor, judicious edge design of the electrode sheet is important for improving the yield of dry electrodes, as grooved or cracked edges must be trimmed prior to the subsequent lamination step. Therefore, edge roughness serves as an effective indicator of dimensional quality in dry electrode fabrication.[31] Edge roughness was quantified from digital images using the following equation:

$$\text{Edge roughness} = \frac{L_p - L}{L}$$

where L is the apparent length of the electrode, and L_p is the measured perimeter length of the edge (Fig. 4(a)).[32] The SDE exhibited numerous large cracks and a rough edge due to its irregular and inhomogeneous fibrous structure, which caused uneven compression during elongation of the free-standing film in the machine direction. In contrast, the DDE retained its original shape without significant edge damage after roll pressing, resulting in a substantially lower edge roughness of 0.17 compared to 0.79 for the SDE (Fig. 4(b)).

In addition to edge stabilisation, the significance of the PTFE rope on the cohesive properties of the electrodes was evaluated by a tensile test. The free-standing DDE film showed a tensile strength of 1.39 N mm^{-2}, approximately three times higher than that of the SDE (0.47 N mm^{-2}) (Fig. 4(c)). Also, a yield strain of the DDE was increased from 0.35% to 0.7%, indicating a more ductile characteristic. Furthermore, the DDE exhibited a higher cohesion force of 3.32 mN mm^{-1} using a 180° tape peel-off test, whereas the SDE showed a lower cohesion force of 1.16 mN mm^{-1} (Fig. 4(d)). The enhanced mechanical strength of the DDE offers significant advantages for stable roll-to-roll manufacturing, minimising the risk of material
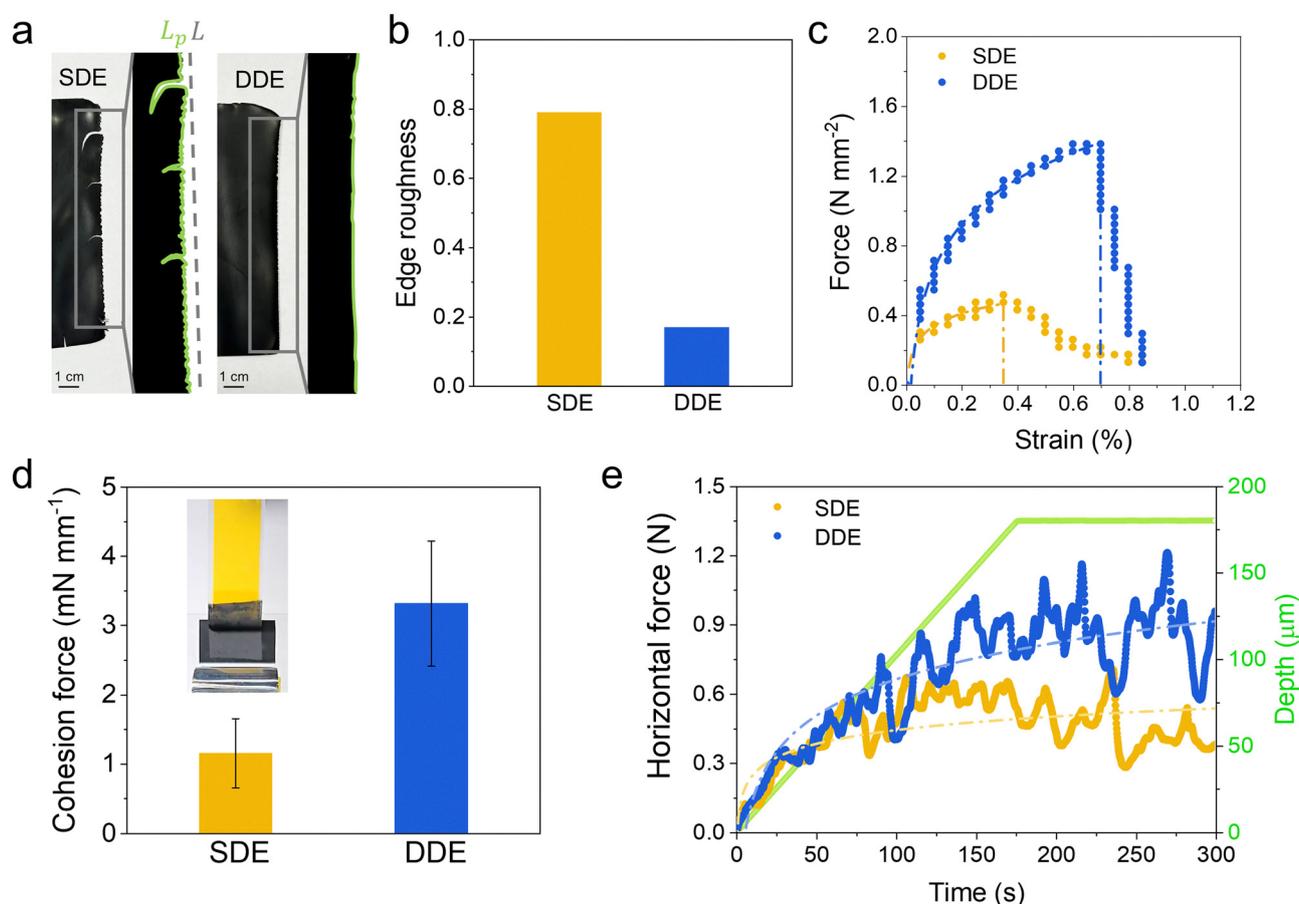

Fig. 4 Mechanical characterization of thick dry electrode. (a) Digital photographs of electrode edge after roll pressing. (b) Edge roughness calculation of as-roll pressed freestanding electrode film. (c) Tensile stress–strain curves of as-roll pressed freestanding electrodes film. The plotted data represent the median result among three independent tests. (d) Cohesion force measured by 180° peel-off test of the freestanding electrode films. Inset shows a photograph of DDE during the peel-off test. (e) Horizontal force and depth profiles measured by SAICAS. Dash–dot lines in (c) and (e) denote background trendlines used for visual guidance.

8452 | *Energy Environ. Sci.*, 2025, **18**, 8446–8461

This journal is © The Royal Society of Chemistry 2025

breakage. To further investigate the mechanical strength of PTFE rope, electrode granules were subjected to an automatic kneader to characterise the required torque during shear mixing (Fig. S7). The SDE required a maximum torque of 52.1 N m, whereas DDE required 56.3 N m, suggesting that PTFE rope possess superior mechanical strength.

Additionally, the DDE was successfully laminated onto a carbon-coated aluminium (c-Al) current collector. The lamination process typically requires high compressive force to bond the free-standing electrode film to the current collector, which can induce electrode cracking due to elongation mismatch between the electrode and current collector. In this context, the SDE exhibited severe macro-cracking near the current collector during lamination, a consequence of its poorly fibrillated PTFE fibre structure. The undeveloped fibrous structure lacked the mechanical resilience to uniformly dissipate external stress across the electrode (Fig. S8a). In contrast, the DDE was laminated successfully without any significant electrode fracture (Fig. S8b).

The as-laminated electrodes were characterised using a surface and interfacial characterisation analysis system (SAICAS) to comprehensively evaluate both adhesion and cohesion strength. During consecutive passes of the angled blade (Fig. S9a), two perpendicular forces—horizontal force (F_h) and vertical force (F_v)—were applied simultaneously to moderately cut the electrode, allowing analysis of inter-particle cohesion within the electrode and adhesion between the electrode and current collector, based on the blade penetration depth.[33] As shown in Fig. 4(e), the DDE exhibited cohesion forces comparable to those of the SDE at the initial cutting stage (depth < 50 μm). However, between 50 μm and 180 μm cutting depth, the SDE displayed a lower horizontal force, indicating inferior cohesion strength. This observation is consistent with the previously discussed SEM images, which revealed macro-cracks at the electrode bottom (as already shown in the Fig. S8a). At cutting depths exceeding 180 μm—corresponding to the electrode thickness—adhesion was assessed. Here, the SDE showed a marked decrease in horizontal force, while the DDE maintained mechanical resistance due to its well-developed interface between the electrode and current collector, without significant macro-crack formation. Additionally, a distinct difference in electrode behaviour during scraping was observed. The SDE exhibited a stiff and straight shape, undergoing consecutive fractures under mechanical stress (Video S1 and Fig. S9b), which is unsuitable for roll-to-roll manufacturing due to the risk of electrode rupture during the winding process.[34,35] In contrast, the DDE followed the scraping direction smoothly, showing no mechanical resistance and demonstrating flexible behaviour under mechanical stress (Video S2 and Fig. S9c). Consequently, the PTFE rope comprising the dual-fibrous structure of the DDE imparts excellent mechanical integrity, making it highly suitable for roll-to-roll manufacturing processes.

Electrochemical characterisation of the DDE

The electrochemical performance of the DDE and SDE was evaluated using 2032-type coin cells. The mass loading of active material in each electrode was designed to be 50.48 mg cm^{-2}. The DDE exhibited an initial discharge capacity of 201 mAh g^{-1}

at a voltage range of 3.0–4.3 V (vs. Li/Li$^+$), corresponding to an areal capacity of 10.1 mAh cm^{-2} (Fig. S10a and b), which surpasses the maximum areal capacity of slurry-based electrodes (8.4 mAh cm^{-2}, Fig. S11a). However, slurry electrodes exceeding this threshold showed mechanical cracks during the drying and calendering process, as detailed in Fig. S11b–d. To ensure a fair comparison between the slurry and dry electrodes, fabrication details of the slurry electrodes are provided in the Experimental section. While both the SDE and DDE exhibited similar initial electrochemical characteristics, the DDE demonstrated markedly superior cycling performance compared to the SDE. As shown in Fig. 5(a), the DDE retained 85.3% of its capacity after 100 cycles, whereas the SDE experienced a sharp decline in capacity after the 60th cycle. This sudden capacity drop is typically attributed to an extreme increase in resistance at the Li metal and to electrolyte depletion. The inhomogeneous reaction of the SDE can continuously generate unbalanced charge distribution onto both positive and negative electrodes.[36,37] Notably, the areal capacity ratio of negative to positive electrode (N/P ratio) in the half cell is theoretically calculated as 4, based on the relevance of thickness and areal capacity of Li metal.[38,39] Given the high Li utilization and unbalanced charge distribution, this failure is likely due to the instability of the Li metal, exacerbated by uneven Li-ion flux and expedited dendritic growth. The SEM images and surface topology of Li metal after 3 cycles clearly show that lithium metal paired with the SDE exhibits more irregular growth compared to that of paired with the DDE (Fig. S12). The degradation mechanism of the DDE will be discussed in detail through full cell cycling and post-mortem analyses.

Meanwhile, electrochemical impedance spectroscopy (EIS) measurements were conducted to analyse the impedance build-up in the DDE and SDE during charge/discharge cycling. As shown in Fig. 5(b) and Fig. S13, the internal bulk resistance (R_b) of the cell—represented by the intercept on the x-axis in the Nyquist plot—increased noticeably in the SDE after only 20 cycles and ultimately led to electrochemical failure after 70 cycles (Fig. S13a) due to excessive dendritic growth and dead lithium passivating the active lithium metal surface. In contrast, the R_b of the DDE remained nearly constant for the first 70 cycles, with only a slight increase observed thereafter (Fig. S13b). Additionally, the charge transfer resistance (R_{ct}), represented by the second semicircle in the Nyquist plot, remained consistently lower in the DDE than in the SDE throughout cycling. This difference is considered to have originated from severe particle cracking in the SDE during repeated charge/discharge cycling (to be discussed in Fig. 6). The discharge rate capability of the DDE was compared to that of the SDE, in which the discharge current densities varied from 0.1C to 0.5C under a constant charge current density of 0.1C (Fig. S14). Both electrodes exhibited almost similar rate performance due to same electrode materials, composition and porosity. Although the DDE exhibited lower impedance than the SDE, the prolong lithium-ion diffusion path through the thick electrode (thickness 180 μm) limited the overall electrochemical kinetics.

Differential capacity analysis at the 1st and 60th charge/discharge states (Fig. S15a and b) was performed to further investigate the degradation mechanisms of the dry electrodes.

This journal is © The Royal Society of Chemistry 2025

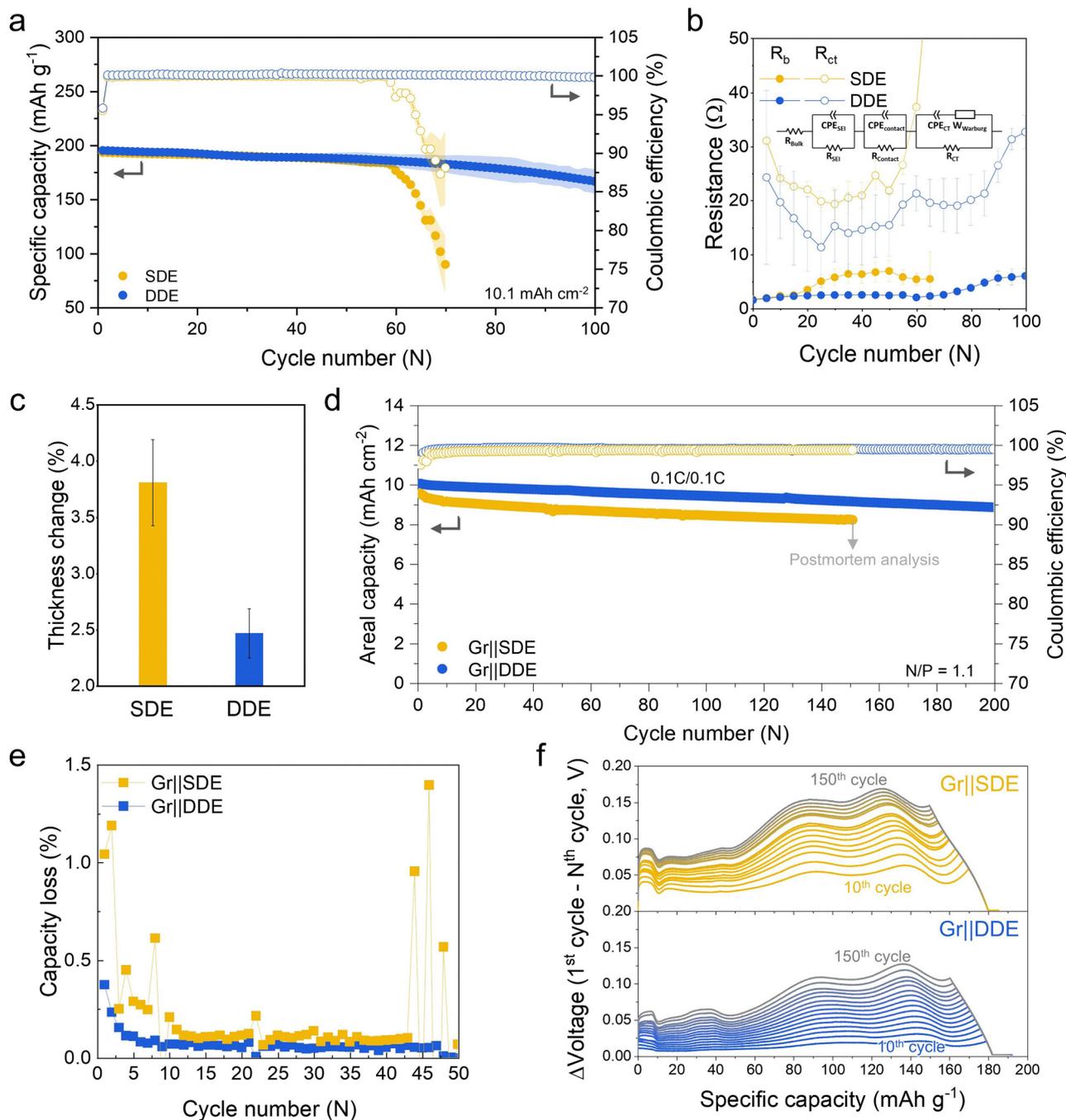*Energy Environ. Sci.*, 2025, **18**, 8446–8461 | **8453**

Fig. 5 Electrochemical characterization of thick dry electrode. (a) Cycle retention of SDE and DDE at a current density of 0.2C/0.2C. (b) Bulk resistance (R_b) and charge transfer resistance (R_{ct}) from EIS measurements as a function of cycle number. Inset shows an associated equivalent circuit diagram to calculate the R_b and R_{ct}. (c) Change of electrode thickness after the electrolyte stability test. (d) Cycle retention of Gr||SDE and Gr||DDE coin full cell at current density of 0.1C/0.1C and (e) corresponding capacity loss during first 40 cycles. (f) Difference of cell voltage of Gr||SDE and Gr||DDE coin full cells between 1st cycle and N^{th} cycle (at 10-cycle intervals).

For the NCM811 electrode, three characteristic oxidation peaks are typically observed during charging, corresponding to the H1 → M (hexagonal to monoclinic), M → H2 (monoclinic to hexagonal), and H2 → H3 (hexagonal to hexagonal) transitions.[40] Notably, the DDE exhibited a significantly smaller peak potential shift (ΔE) compared to the SDE (Fig. S15c and d). For the H1 → M transition during charging, the ΔE of the SDE

was 0.08 V, whereas the DDE showed a minimal shift of only 0.006 V, indicating negligible impedance build-up. During discharge, the ΔE associated with the H3 → H2 transition was 0.07 V for the SDE and 0.053 V for the DDE. Moreover, both the ΔE values and the reduction in peak intensity were markedly more severe in the SDE across all phase transitions during discharge.

8454 | Energy Environ. Sci., 2025, 18, 8446–8461

This journal is © The Royal Society of Chemistry 2025

Although PTFE intrinsically exhibits a non-swelling nature in polar organic solvents due to its extremely low polarity and surface energy, the fibrillated PTFE structure in the DDE can retain liquid electrolytes owing to its increased surface area.[24] Since PTFE fibres physically secure the electrode components without forming chemical interactions, the presence of liquid electrolyte may weaken the binding force between electrode components, potentially leading to electrode swelling and degradation of the electronic transport network. To assess the impact of electrolyte exposure on the mechanical stability of the electrodes, an electrolyte stability test was performed by monitoring the thickness change before and after soaking in dimethyl carbonate (DMC) (Fig. 5(c)). After soaking, a rinse process was applied to remove any detached electrode fragments. The SDE exhibited irregular bulging and a thickness increase of 3.82% due to electrolyte penetration and structural inhomogeneity (Fig. S16a), whereas the DDE displayed no irregular volume expansion and a thickness change of only 2.47% (Fig. S16b), which is notably lower than previously reported values for PTFE-based dry electrodes.[41] Furthermore,
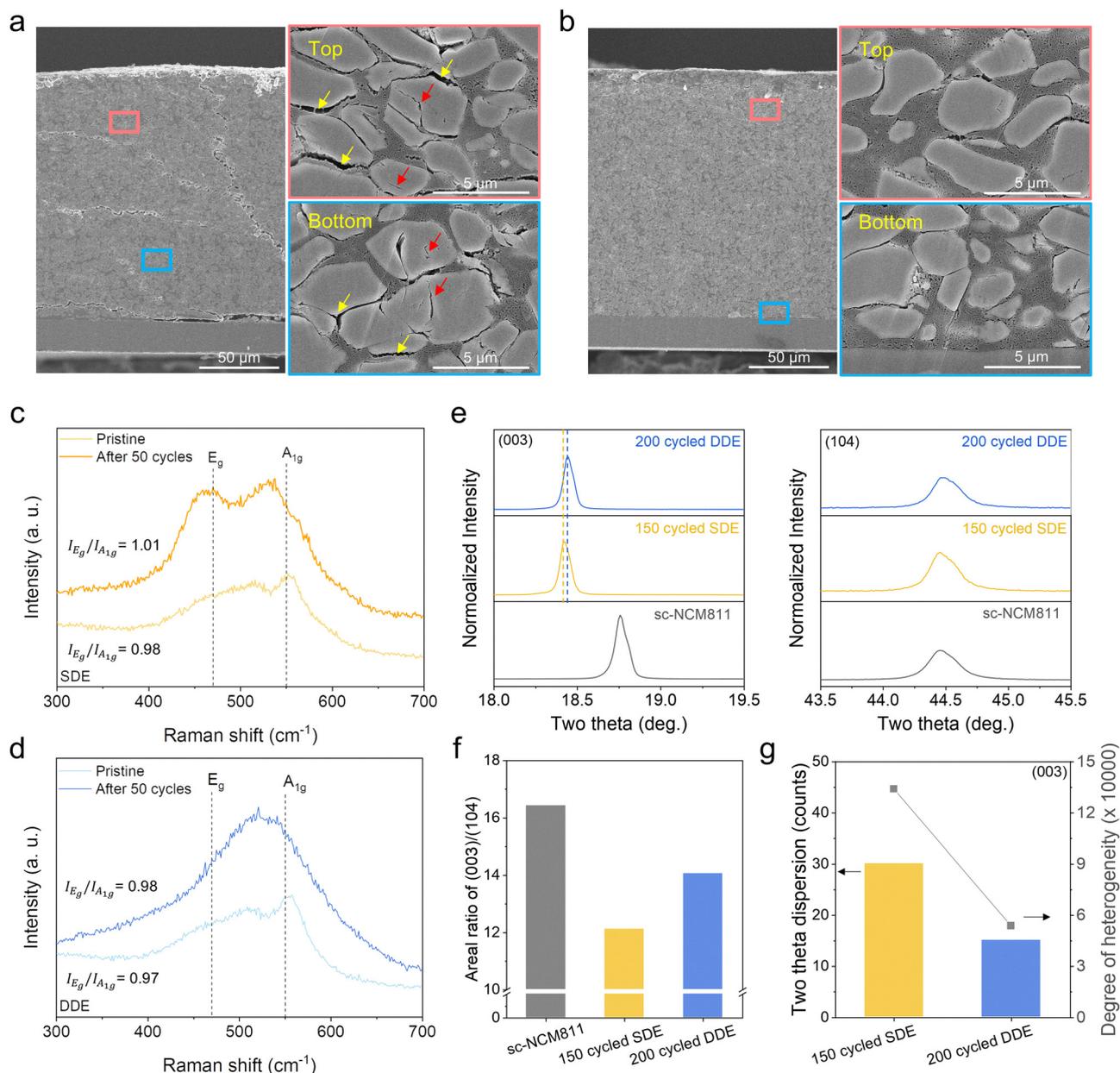

Fig. 6   Post-mortem investigation of electrode stability after cycling. Ion-milled cross-sectional SEM images of (a) SDE and (b) DDE after 50 cycles in half cells. Red arrows and yellow arrows indicate particle cracks and isolation of active materials from PTFE-CB domain, respectively. Raman spectroscopy of (c) SDE and (d) DDE at the surface after 50 cycles in half cells. (e) XRD patterns corresponding to (003) and (104) planes of SC-NCM811, investigated through cycled electrodes of full cells pairing with graphite negative electrode. Calculated results to confirm electrode degradation through the comparison of (f) areal ratio (003)/(104) and (g) degree of heterogeneity.

the SDE was partially fractured during the electrolyte soaking and mechanical vortexing (Fig. S16a).

To further investigate the degradation mechanism and demonstrate the feasibility of practical application, the electrochemical performance of the Gr||DDE coin full cell was evaluated with an N/P ratio of 1.1. To achieve a high mass loading comparable to the thick DDE, Gr anodes were fabricated *via* a slurry-based double-casting technique (details are provided in the Experimental section). The as-prepared Gr anodes exhibited a well-developed electrode structure and a reversible specific capacity with a high arealcapacity of 10.89 mAh cm^{-2} (Fig. S17). The Gr||DDE coin full cell demonstrated excellent cycling performance, with a capacity retention of 88.1% after 200 cycles (Fig. 5(d)), whereas the Gr||SDE coin full cell showed a capacity retention of 85.3% after 150 cycles at the current density of 0.1C/0.1C with the cut-off voltage of 2.7–4.25 V. While no significant capacity difference was observed between the SDE and the DDE up to the 60th cycle in the half cell configuration (Fig. 5(a)), a noticeable capacity loss was observed in the Gr||SDE full cell (Fig. 5(e)). This discrepancy suggests that the degradation of DDE is primarily driven by the loss of Li inventory during cycling, as reported in many previous studies.[42–44] The unbalanced charge kinetics and weak mechanical integrity of the SDE exacerbate sc-NCM811 particle cracking, leading to transition metal (TM) dissolution and cation mixing (to be discussed in Fig. 6). The TM dissolution induces continuous reformation of the solid electrolyte interphase (SEI) at the anode surface, consuming active Li. The resulting Li inventory loss leads to electrode slippage,[42] which in turn causes severe cell polarisation in the SDE compared to the DDE (Fig. 5(f) and Fig. S18).

Confirmation of reaction uniformity for cycled electrode

Electrochemical evaluation revealed a distinct difference in cycling behaviour between the DDE and SDE, despite both dry electrodes being fabricated from the same materials and composition, differing only in the fabrication process. To investigate the origin of these performance discrepancies, post-mortem analyses were conducted with a focus on microstructural homogeneity and variations in the degradation of sc-NCM811 particles. The SDE electrode exhibited a non-uniform structure due to insufficient fibrillation of PTFE and particle agglomeration during fabrication, which can induce localised reactions within the electrode as discussed in the LEIS analysis (Fig. 3(e)), thereby amplifying the heterogeneity in the degradation of individual sc-NCM811 particles during cycling. As shown in the cross-sectional SEM image (Fig. 6(a) and (b)), the SDE showed signs of particle cracking after cycling (red arrow) and loss of interparticle contact (yellow arrow). Notably, the SDE showed numerous and severe particle cracks throughout the electrode compared to the DDE (Fig. S19). The inhomogeneous reaction behaviour could gradually induce degradation disparity of particles in the electrode. Therefore, individual sc-NCM811 particles might undergo various depths of electrochemical reactions. This can lead to charge localisation and particle cracking within certain particles (Fig. S19a),

consequently posing a risk of accelerating TM dissolution or cation mixing. By contrast, the DDE exhibited negligible particle degradation owing to dual-fibrous PTFE-driven well-distributed charge transport and sturdy cohesion through the electrode (Fig. S19b). In this regard, the heterogeneity of the SDE disrupted charge balance across the electrode, resulting in severe degradation characterised by pronounced particle fractures.

Non-uniform electrochemical reactions within the electrode lead to unbalanced charge kinetics and variations in the state of charge (SOC) among individual sc-NCM811 particles, as briefly unveiled by morphological observation of cycled electrodes. To deeply investigate the relationship between electrochemical degradation and reaction homogeneity, Raman spectroscopy was employed to assess the degree of particle degradation within the electrode. Typically, TMs in the NCM811 exhibit two characteristic Raman-active modes: the A_{1g} mode, corresponding to metal–oxygen stretching vibrations along the *c*-axis, and the E_g mode, associated with metal–oxygen–metal bending vibrations in the *a/b* plane.[45,46] Particle degradation caused by cation mixing or TM dissolution hinders the reversible accommodation of Li ions between oxygen atoms, resulting in a shift or reduction in the A_{1g} peak intensity. Therefore, the intensity ratio of E_g to A_{1g} (E_g/A_{1g}) can directly reflect the extent of degradation related to structural deformation of the NCM811 crystal during cycling. To evaluate heterogeneity in reaction and degradation behaviour, pristine and 50-cycled electrodes were analysed at the fully discharged state. As shown in Fig. 6(c), the SDE exhibited an increase in the E_g/A_{1g} intensity ratio from 0.98 to 1.01 after cycling, which implies more structural destruction. This continuous consumption of active Li might result in Li inventory loss and capacity decay in the full cell configuration as already discussed in the Fig. 5(d). In contrast, the DDE maintained a nearly unchanged intensity ratio before and after cycling (0.97 → 0.98), despite the high mass loading and electrode thickness (Fig. 6(d)). The uniform distribution of PTFE–CB domains facilitated homogeneous charge kinetics across the electrode, minimising structural degradation.

The SDE and DDE were further investigated using X-ray diffraction (XRD) analysis, extracted from the full cells of Gr||SDE and Gr||DDE, after cycles. Magnified XRD patterns corresponding to the (003) and (104) planes of sc-NCM811 are shown in Fig. 6(e). After 150 cycles, the SDE exhibited a more pronounced shift in the (003) peak compared to the DDE after 200 cycles in the full cell configuration, which indicate that less active Li was inserted after the end of discharge. Meanwhile, the areal ratio of (003)/(104) clearly demonstrated structural degradation of the electrode where the value determines cationic disorder in crystal structure by cation mixing and particle cracking.[47] Compared to the pure sc-NCM811, cycled electrodes showed a lower areal ratio of (003)/(104) meaning inevitable structural deformation by repeated Li-ion insertion/extraction during cycling (Fig. 6(f)). Nevertheless, the DDE persisted in its original structure during long-term cycling with relatively lower structural distortion. In addition, the peaks of (003) were delicately deconvoluted, as shown in Fig. S20, to calculate the degree of heterogeneity and obviously demonstrate the

8456 | *Energy Environ. Sci.*, 2025, **18**, 8446–8461

This journal is © The Royal Society of Chemistry 2025

importance of electrode homogeneity and manufacturing process as a structural factor to directly influences material degradation. The calculation based on XRD analyses was proceeded through equations as below:

$$x_m(\text{weighted mean, mean peak position}) = \frac{\sum x_n w_n}{A}$$

$$\sigma_i(\text{weighted deviation}) = \sum w_n \times (x_m - x_n)^2$$

$$\sigma_i^2(\text{weighted variance}) = \frac{\sum w_n \times (x_m - x_n)^2}{A}$$

where x_n and w_n indicate the highest intensity and its areas for each deconvoluted peak, derived from (003) plane of XRD patterns. Deviation, denoted as σ_i, means the dispersion of two-theta reflecting the variety of particle population after cycles. Variance, σ_i^2, quantifies the degree of heterogeneity, derived from localised charge distribution during the electrochemical reaction.

Fig. 6(g) consequently showed calculated values of dispersion and heterogeneity of the SDE and DDE after cycles. The higher dispersion of two-theta was attributed to non-uniform particle states implying the presence of barely reacted particles and severe particle collapse by locally excessive Li-ion extraction. In contrast, the DDE relatively enabled uniform electrochemical reaction for each particle even with a higher number of cycles, consistent with a sharp peak structure and narrow peak distribution. Therefore, the DDE featured a lower degree of heterogeneity after cycling demonstrating that higher structural homogeneity. According to comprehensive exploration of cycled electrodes, SDE and DDE showed distinct structural degradation at the electrode level even though both electrodes were designed by same material components excluding fabrication process. While we carefully suggest that electrode degradation arises from various mechanisms, such as structural collapse, cation mixing, and lithium inventory loss, identifying the exact causes and quantifying their relative contributions are beyond the scope of this study.

Practical pouch cell-level evaluation

For large-scale roll-to-roll production of dry electrodes, various process parameters should be considered, including thickness control, powder feeding, and reproducibility. To confirm the scalability of our process and the benefits of ultra-high-areal-capacity electrodes, we implemented our DDEs in a 1.2 Ah stacked pouch full cell *versus* a Li metal anode, as shown in Fig. 7(a). The DDE positive electrodes and Li metal negative electrodes were prepared in a 5/6 (positive/negative) layer configuration. In terms of electrochemical performance, the Li||DDE stacked pouch cell exhibited a high initial Coulombic efficiency (ICE) of 92.1% and a cell capacity of 1.25 Ah, despite the use of a high-loaded DDE positive electrode (10.1 mAh cm^{-2}). Owing to the high areal capacity of the DDE, the Li||DDE pouch cell achieved a gravimetric energy density of 349 Wh kg$_{cell}^{-1}$ and a volumetric energy density of 800 Wh L$_{cell}^{-1}$ (Fig. 7(b) and Table S1). However, the Li||DDE pouch cell exhibited limited cycle retention (Fig. S21a), primarily due to the instability of the

Li metal in high-areal-capacity cells, consistent with observations in the coin half cell results and previous studies.[48] To clarify the reason of short cycle life, the Li||DDE pouch cell was disassembled. A significant amount of lithium metal detached from lithium metal negative electrode and adhered to the separator during disassembling due to dendrite growth (Fig. S21b). In addition, DDE positive electrodes were extracted from the and reassembled into coin half cells with fresh Li metal and electrolyte. Notably, the reassembled cell exhibited stable electrochemical performance, indicating no intrinsic degradation of DDE (Fig. S21c).

Therefore, we subsequently tested a Gr||DDE stacked pouch cell using the same 5/6 (positive/negative) stack layer configuration. To further highlight its practical advantages, the jelly roll of the Gr||DDE cell was compared with that of a Gr||NCM811 control cell, which was prepared using a conventional slurry-based wet process and designed with a standard electrode areal capacity of 3.2 mAh cm^{-2}. This reference stacked pouch cell requires 17/18 (positive/negative) stack layers to achieve a 1.2 Ah-class capacity, whereas the DDE achieved the same capacity with only 5/6 stack layers. By minimising inactive components such as current collectors and separators, the Gr||DDE cell demonstrated a 19% reduction in jelly roll thickness (6.07 mm → 4.92 mm) and a 23% reduction in mass (15.3776 g → 11.8848 g), as shown in Fig. 7(c) and Fig. S22a, b. A comparison of component mass and thickness in the pouch cells clearly highlights the advantage of high-areal-capacity electrode in reducing overall cell weight and dimensions (Fig. 7(d)). Owing to these practical advantages at the cell-level, the Gr||DDE stacked pouch full cell delivered a gravimetric energy density of 291 Wh kg$_{cell}^{-1}$ and a volumetric energy density of 685 Wh L$_{cell}^{-1}$, representing improvements of 16% and 11%, respectively, over the conventional slurry pouch cell of 251 Wh kg$_{cell}^{-1}$ and 618 Wh L$_{cell}^{-1}$. The Gr||DDE full cell fulfilled the designed specifications, achieving an initial Coulombic efficiency of 90.2% and a reversible capacity of 1.23 Ah, with negligible electrochemical deviation from the coin full cell (Fig. S23). Driven by the excellent reaction homogeneity and mechanical integrity of the DDE, the Gr||DDE pouch full cell exhibited stable cycle retention of 80.2% after 600 cycles at 0.2C (Fig. 7(e)). Meanwhile, the cell showed negligible capacity decay and no significant increase in overpotential (Fig. S24) except during initial the 10 cycles, which is mainly attributed to SEI formation and cell polarization.[57,58] As a result, it is noteworthy that the 1.2 Ah-class Gr||DDE pouch full cell exhibited the highest cell capacity and cyclability, along with outstanding areal capacity and energy density, among previously reported pouch-type full cell utilising DBEs (Fig. 7(f) and Table S2).[48–56] Furthermore, the DDE exhibited one of the highest areal capacities, not only surpassing previously reported PTFE-based dry electrodes, but also outperforming various other dry electrode strategies such as PVDF hot-melting, thermoplastic binders, and graphene-based binder-free scaffold, which suffer from limited processability and scalability (Table S3). These achievements underscore the critical importance of the design of both electrically
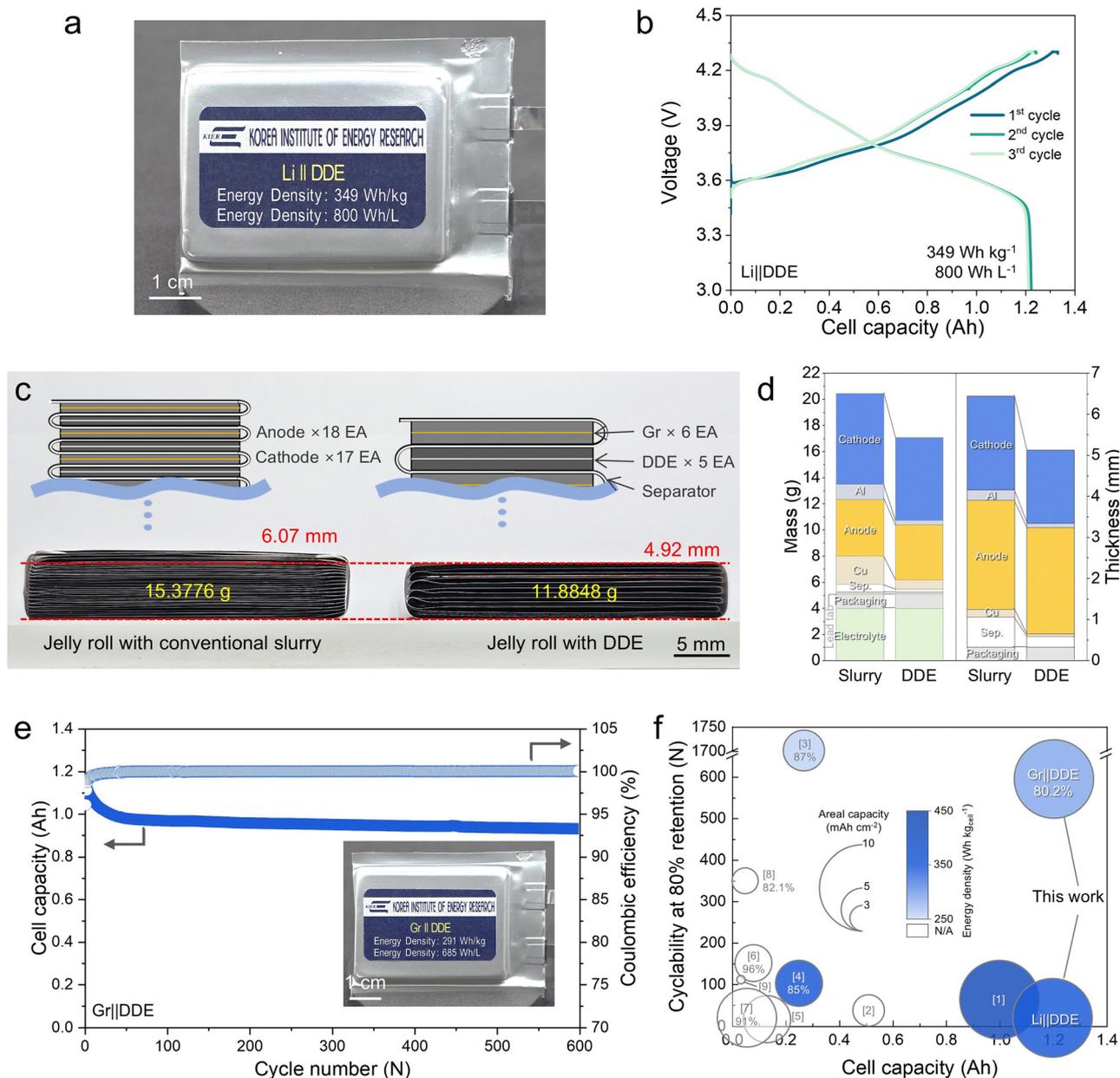
This journal is © The Royal Society of Chemistry 2025

Energy Environ. Sci., 2025, **18**, 8446–8461 | **8457**

Fig. 7 Practical demonstration of DDE using 1.2 Ah-class pouch cell. (a) Photograph of 1.2 Ah-class Li‖DDE pouch full cell. (b) Initial galvanostatic charge/discharge formation profile of Li‖DDE pouch full cell. (c) A photograph comparing side view of 1.2 Ah-class jelly rolls composed of Gr‖DDE and conventional slurry electrodes. Inset represents the corresponding schematic image showing cell stack configuration. (d) Comparison of the mass and thickness of individual components in Slurry-based and DDE-based pouch cells. (e) Cycle retention of Gr‖DDE pouch full cell at 0.2C/0.2C. Inset shows a photograph of Gr‖DDE pouch full cell. (f) Performance comparison of dry electrode using pouch-type cell configuration in terms of four parameters: cell capacity (x-axis), cyclability at 80% of retention (y-axis), areal capacity of the electrode (diameter), and gravimetric energy density (heatmap). The number assigned to each circle corresponds to the serial number in Table S2 (ref. 48 and 49–56).

conductive and mechanically resilient binder networks in dry-coated electrodes for realising high-energy and stable battery systems, alongside advancements in electrode design. Meanwhile, given the growing regulatory on per- and poly fluoroalkyl substances (PFAS) materials, including PTFE, the use of fluorinated polymers raises potential environmental and policy-related concerns. Accordingly, future studies should explore the development of fluorine-free polymer binders as well as effective recycling strategies for PTFE to ensure both

technological viability and regulatory compliance in battery manufacturing.

Conclusions

In summary, we demonstrated a dual-fibrous PTFE structure that enables the fabrication of homogeneous and mechanically robust dry electrodes through systematic control of the processing parameters. The multi-step grinding and kneading process

8458 | *Energy Environ. Sci.*, 2025, **18**, 8446–8461

This journal is © The Royal Society of Chemistry 2025

produced a distinctive PTFE fibrous structure comprising thin PTFE fibres and thick PTFE ropes, which collectively ensured uniform material distribution and enhanced mechanical integrity. Comprehensive macroscopic and microscopic analyses confirmed the superior component homogeneity of the DDE driven by well-distributed PTFE fibres, which contributed to improved electrochemical performance compared to conventional dry electrodes fabricated *via* single-step fibrillation. The unique PTFE rope exhibited outstanding mechanical properties—including reduced edge roughness, improved cohesion/adhesion forces, and enhanced tensile strength—which are critical engineering factors for roll-to-roll manufacturing. As a result, the DDE delivered a high areal capacity of 10.1 mAh cm^{-2} with stable cycling retention. Its excellent electrochemical reaction homogeneity and mechanical stability mitigated the degradation of sc-NCM811 during repeated charge/discharge cycles. Consequently, the DDE pouch full cell, paired with a Li metal, achieved a high energy density of 349 Wh kg^{-1} and 800 Wh L^{-1}. As a practical demonstration, the Gr||DDE stacked pouch full cell exhibited stable cycle retention of 80.2% after 600 cycles, outperforming previously reported dry electrodes. We conclude that the dual-fibrous PTFE-based dry electrode represents a promising and versatile platform technology for advanced lithium batteries and cost-effective battery manufacturing.

Experimental

Fabrication of dry electrode and control slurry electrode

The DDE was fabricated through a multi-step fibrillation process consisting of mixing, first kneading, grinding, second mixing, second kneading, film formation, roll pressing, and laminating. A powder mixture comprising sc-NCM811 (SML83-L15U, SM LAB), PTFE (F-104, DAIKIN), and CB (SUPER C65, TIMCAL) in a weight ratio of 90:1:7 was initially mixed using a planetary mixer (ARE-310, THINKY), followed by first kneading with a mortar and pestle manually. The resulting electrode dough was then ground and remixed using the planetary mixer with an additional 2 wt% PTFE. After the second kneading, the dough was subjected to the formation of free-standing electrode film (Atlas 180, MARCATO), followed by roll pressing (EN-SP1015, ENNEX). Finally, the prepared electrode film was laminated onto a c-Al current collector. The SDE was fabricated using a simplified fibrillation process involving only mixing and first kneading. A powder mixture of sc-NCM811 (SML83-L15U, SM LAB), PTFE (F-104, DAIKIN), and CB (SUPER C65, TIMCAL) in a weight ratio of 90:3:7 was mixed using the planetary mixer (ARE-310, THINKY), followed by manual kneading with a mortar and pestle. All subsequent processing steps were identical to those used for the DDE.

The control slurry electrode was prepared by mixing sc-NCM811, PVdF (KF9700, KUREHA), and CB at a weight ratio of 94:3:3 in NMP. The resulting slurry was cast onto Al foil and subjected to solvent drying at 120 °C for 12 h under vacuum. The Gr anode was prepared using a double-casting method with two distinct binders. The bottom layer, composed of Gr

(PAS-CP1, POSCO), PVdF, and CB (96:3:1, w:w:w) was dispersed in NMP and cast onto copper foil, followed by solvent drying at 120 °C for 12 h under vacuum. The top layer, consisting of Gr, styrene-butadiene rubber (SBR, BM 480B, ZEON), carboxymethyl cellulose (CMC, Daicel 2200, DAICEL), and CB (96:2:1:1, w:w:w:w), was dispersed in deionised water and cast directly onto the dried bottom layer. This was followed by solvent drying at 110 °C for 6 h under vacuum.

Physicochemical/mechanical characterisation

Electrode microstructures were observed using field-emission scanning electron microscopy (FE-SEM, Regulus 8100, HITACHI), and elemental distribution mapping was conducted *via* energy-dispersive X-ray spectroscopy (EDS, Ultim Max 100, OXFORD). Cross-sectional samples were prepared using a cross-section polisher (Model 1061 SEM Mill, INTEC). Pore size distributions were analysed using a mercury intrusion porosimeter (AutoPore IV, Micromeritics), and electrical resistivity was measured with a resistivity meter (RSD-1G, DASOLENG). Three-dimensional surface morphology was characterised using a 3D optical profiler (S Neox, SENSOFAR) over an area of 338 μm (x) × 283 μm (y). Macroscopic and local structural uniformities were assessed using X-ray micro-computed tomography (Micro-CT, Vtomex M300, Baker Hughes) with a scanned domain of 954 μm (x) × 622 μm (y) × 122 μm (z) with voxel size of 650 nm. Solid volume fraction mapping along the vertical axis of the electrodes were quantified using MatDict module in the image processing software (GeoDict2024, Math2-Market GmbH). Mechanical properties of the dry electrodes were evaluated using a universal testing machine (UTM, UTM-2020, MYUNGJI TECH) and a surface and interfacial cutting analysis system (SAICAS, EN-EX, DAIPLA WINTES). To clear data interpretation, we provided the background trendlines featured in Microsoft Excel. For SAICAS measurements, the blade was operated at a horizontal speed of 10 μm s^{-1} and a vertical speed of 1 μm s^{-1}. The shear torque of electrode granules was measured using a kneader (KND-0.5P, KM Tech) under 10 rpm of blade rotation. Post-mortem analyses after cycling were performed using Raman spectroscopy (alpha300R, WITec) with a 532 nm laser and X-ray diffraction (XRD, SmartLab SE, Rigaku) utilising Cu Kα radiation.

Fabrication of coin and pouch cells

The electrochemical performance of the electrodes was evaluated using 2032-type coin cells. For half cell configurations, Li metal (thickness = 200 μm) served as the reference and counter electrode, paired with a polyethene (PE) separator (thickness = 20 μm). The Gr||DDE coin full cell consisted of an sc-NCM811 positive electrode and a double-cast Gr negative electrode, using the same PE separator. Electrolytes used in this study were 1.3 M lithium hexafluorophosphate (LiPF$_6$) in ethylene carbonate (EC)/ethyl methyl carbonate (EMC)/dimethyl carbonate (DMC) at a volume ratio of 1:1:1, with 10 wt% fluoroethylene carbonate (FEC) and 1 wt% lithium difluoro(oxalato)borate (LiDFOB) for cells paired with Li metal anodes. For cells paired with Gr anodes, the electrolyte consisted of 1.3 M LiPF$_6$ in EC/EMC/

DMC (1:1:1, v:v:v) with 2 wt% vinylene carbonate (VC) and 1 wt% LiDFOB. Stacked pouch full cells—including Gr‖DDE, Li‖DDE, and Gr‖Slurry-cast sc-NCM811 configurations—were assembled using a PE separator (thickness = 20 μm) and sealed in an Al-laminated pouch film. Note that Li metal was adopted in pouch cell configuration with the thickness of 100 μm. The electrolyte-to-capacity (E/C) ratio was maintained at 3.2 g Ah^{-1}, and cell assembly was conducted in a dry room with a dew point of −60 °C. Electrochemical performance of the pouch-type cells was evaluated at 25 °C under a constant stack pressure of 100 kPa. The specific energy densities of the stacked pouch cells were calculated based on the total mass or volume of the assembled cells, including the anode, separator, electrolyte, packaging film, lead tab, and other components.

Electrochemical characterisation

The electrochemical performance was evaluated using a cycle tester (WBCS3000L for coin cells and WBCS3000M for pouch cells, WonATech) under various charge/discharge conditions. All electrochemical characterisations were performed after three initial formation cycles at 0.05C/0.05C (charge/discharge). EIS of coin cells was conducted at the fully lithiated state over a frequency range of 10^6 to 10^{-1} Hz with an applied amplitude of 10 mV (VSP-300, Bio-Logic). Electrolyte stability was assessed by soaking the electrode in DMC for 7 days, followed by mechanical vortexing, rinsing, and drying. LEIS was carried out using an M470 scanning probe workstation (Bio-Logic). Measurements were performed at 100 Hz with an applied amplitude of 100 mV and a probe spacing of 10 μm. Prior to LEIS analysis, electrodes were charged to a SOC of 50% after the formation cycles. All measurements were conducted in a beaker-type analytical cell (μTricell, Bio-Logic) using 4 M lithium bis(fluorosulfonyl)imide (LiFSI) in FEC as the liquid electrolyte.

Author contributions

Kwon-Hyung Lee: conceptualization, data curation, formal analysis, investigation, methodology, project administration, visualization, writing – original draft, writing – review & editing. Hyeongseok Shim: conceptualization, data curation, formal analysis, investigation, methodology, writing – original draft, writing – review & editing. Sang Hyun Lee: conceptualization, data curation. Hyeong-Jong Kim: formal analysis. Chanhyun Park: formal analysis. Jingyu Choi: formal analysis. Seok-Ju Lee: formal analysis, Young-Kuk Hong: formal analysis. Jihong Lyu: formal analysis. Jin Chul Kim: formal analysis. Sijeong Park: formal analysis. Hyungyeon Cha: data curation, formal analysis. Wooyoung Jin: data curation, formal analysis. Jinsu Kim: resources. Sinho Choi: resources. Sang-Young Lee: formal analysis. Sung-Kyun Jung: formal analysis. Michael De Volder: data curation, resources, writing – review & editing, Tae-Hee Kim: data curation, resources, supervision, writing – review & editing. Gyujin Song: data curation, formal analysis, funding acquisition, investigation, project administration, supervision, writing – original draft, writing – review & editing.

Conflicts of interest

There are no conflicts to declare.

Data availability

The data supporting the findings of this study are available from the authors upon reasonable request.

Supplementary information is available. See DOI: https://doi.org/10.1039/d5ee03240g

Acknowledgements

Notes and references

1 R. Schmuch, R. Wagner, G. Hörpel, T. Placke and M. Winter, *Nat. Energy*, 2018, **3**, 267–278.

2 J. Liu, Z. Bao, Y. Cui, E. J. Dufek, J. B. Goodenough, P. Khalifah, Q. Li, B. Y. Liaw, P. Liu, A. Manthiram, Y. S. Meng, V. R. Subramanian, M. F. Toney, V. V. Viswanathan, M. S. Whittingham, J. Xiao, W. Xu, J. Yang, X.-Q. Yang and J.-G. Zhang, *Nat. Energy*, 2019, **4**, 180–186.

3 Y. Cao, M. Li, J. Lu, J. Liu and K. Amine, *Nat. Nanotechnol.*, 2019, **14**, 200–207.

4 A. Kwade, W. Haselrieder, R. Leithoff, A. Modlinger, F. Dietrich and K. Droeder, *Nat. Energy*, 2018, **3**, 290–300.

5 Y. Li, Y. Wu, Z. Wang, J. Xu, T. Ma, L. Chen, H. Li and F. Wu, *Mater. Today*, 2022, **55**, 92–109.

6 Y. Lu, C.-Z. Zhao, H. Yuan, J.-K. Hu, J.-Q. Huang and Q. Zhang, *Matter*, 2022, **5**, 876–898.

7 Y. Liu, R. Zhang, J. Wang and Y. Wang, *iScience*, 2021, **24**, 102332.

8 K.-H. Pettinger and W. Dong, *J. Electrochem. Soc.*, 2016, **164**, A6274–A6277.

9 C. Yuan, Y. Deng, T. Li and F. Yang, *CIRP Ann.*, 2017, **66**, 53–56.

10 Y. S. Zhang, N. E. Courtier, Z. Zhang, K. Liu, J. J. Bailey, A. M. Boyce, G. Richardson, P. R. Shearing, E. Kendrick and D. J. L. Brett, *Adv. Energy Mater.*, 2021, **12**, 2102233.

11 J. Kumberg, M. Müller, R. Diehm, S. Spiegel, C. Wachsmann, W. Bauer, P. Scharfer and W. Schabel, *Energy Technol.*, 2019, **7**, 1900722.

12 S. Jaiser, J. Kumberg, J. Klaver, J. L. Urai, W. Schabel, J. Schmatz and P. Scharfer, *J. Power Sources*, 2017, **345**, 97–107.

13 W. B. Hawley and J. Li, *J. Energy Storage*, 2019, **25**, 100862.

14 J. Mun, T. Song, M. S. Park and J. H. Kim, *Adv. Mater.*, 2025, e2506123, DOI: 10.1002/adma.202506123.

15 S. A. Han, J. H. Suh, M.-S. Park and J. H. Kim, *Electrochem. Energy Rev.*, 2025, **8**, 5, DOI: 10.1007/s41918-41025-00240-41915.

8460 | *Energy Environ. Sci.*, 2025, **18**, 8446–8461

This journal is © The Royal Society of Chemistry 2025

16 W. Jin, G. Song, J. K. Yoo, S. K. Jung, T. H. Kim and J. Kim, *ChemElectroChem*, 2024, **11**, e202400288.

17 R. Tao, B. Steinhoff, X.-G. Sun, K. Sardo, B. Skelly, H. M. Meyer, C. Sawicki, G. Polizos, X. Lyu, Z. Du, J. Yang, K. Hong and J. Li, *Chem. Eng. J.*, 2023, **471**, 144300.

18 H. Oh, G.-S. Kim, B. U. Hwang, J. Bang, J. Kim and K.-M. Jeong, *Chem. Eng. J.*, 2024, **491**, 151957.

19 T. Kitamura, S. Okabe, M. Tanigaki, K. I. Kurumada, M. Ohshima and S. I. Kanazawa, *Polym. Eng. Sci.*, 2004, **40**, 809–817.

20 J. Shin, J. H. Lee, J. K. Seo, W. T. A. Ran, S. M. Hwang and Y. J. Kim, *Int. J. Energy Res.*, 2022, **46**, 16061–16074.

21 W. Yao, M. Chouchane, W. Li, S. Bai, Z. Liu, L. Li, A. X. Chen, B. Sayahpour, R. Shimizu, G. Raghavendran, M. A. Schroeder, Y.-T. Chen, D. H. S. Tan, B. Sreenarayanan, C. K. Waters, A. Sichler, B. Gould, D. J. Kountz, D. J. Lipomi, M. Zhang and Y. S. Meng, *Energy Environ. Sci.*, 2023, **16**, 1620–1630.

22 K. Kwon, J. Kim, S. Han, J. Lee, H. Lee, J. Kwon, J. Lee, J. Seo, P. J. Kim, T. Song and J. Choi, *Small Sci.*, 2024, **4**, 2300302.

23 J. Kim, K. Park, M. Kim, H. Lee, J. Choi, H. B. Park, H. Kim, J. Jang, Y. H. Kim, T. Song and U. Paik, *Adv. Energy Mater.*, 2024, **14**, 2303455.

24 G. A. B. Matthews, S. Wheeler, J. Ramírez-González and P. S. Grant, *Front. Energy Res.*, 2024, **11**, 1336344.

25 X. Wang, S. Chen, K. Zhang, L. Huang, H. Shen, Z. Chen, C. Rong, G. Wang and Z. Jiang, *Materials*, 2023, **16**, 7232.

26 T. Tomkovic and S. G. Hatzikiriakos, *Can. J. Chem. Eng.*, 2020, **98**, 1852–1865.

27 A. Zhang, J. Chai, C. Yang, J. Zhao, G. Zhao and G. Wang, *Mater. Des.*, 2021, **211**, 110157.

28 J. Chai, G. Wang, A. Zhang, X. Li, Z. Xu, J. Zhao and G. Zhao, *Chem. Eng. J.*, 2023, **461**, 141971.

29 J. Zhang, J. Sun, H. Huang, C. Ji, M. Yan and Z. Yuan, *Appl. Energy*, 2024, **373**, 123900.

30 U.S. Department of Energy, https://www.energy.gov/sites/default/files/2016/02/f30/QTR2015-6K-Roll-to-Roll-Processing.pdf, (accessed May 2025).

31 T. Jansen, M. Kandula, S. Hartwig, L. Hoffmann, W. Haselrieder and K. Dilger, *Batteries*, 2019, **5**, 73.

32 K. H. Lee, S. W. Kim, M. Kim, D. B. Ahn, Y. K. Hong, S. H. Kim, J. S. Lee and S. Y. Lee, *Adv. Energy Mater.*, 2023, **13**, 2204327.

33 B. Son, M. H. Ryou, J. Choi, T. Lee, H. K. Yu, J. H. Kim and Y. M. Lee, *ACS Appl. Mater. Interfaces*, 2014, **6**, 526–531.

34 J.-H. Kim, N.-Y. Kim, Z. Ju, Y.-K. Hong, K.-D. Kang, J.-H. Pang, S.-J. Lee, S.-S. Chae, M.-S. Park, J.-Y. Kim, G. Yu and S.-Y. Lee, *Nat. Energy*, 2025, **10**, 295–307.

35 A. Schilling, J. Schmitt, F. Dietrich and K. Dröder, *Energy Technol.*, 2016, **4**, 1502–1508.

36 J. Y. Seo, S. Kim, J. H. Kim, Y. H. Lee, J. Y. Shin, S. Jeong, D. W. Sung, Y. M. Lee and S. Y. Lee, *Nat. Commun.*, 2024, **15**, 10134.

37 K. G. Naik, D. Chatterjee and P. P. Mukherjee, *ACS Appl. Mater. Interfaces*, 2022, **14**, 45308–45319.

38 H. Chen, Y. Yang, D. T. Boyle, Y. K. Jeong, R. Xu, L. S. de Vasconcelos, Z. Huang, H. Wang, H. Wang, W. Huang, H. Li, J. Wang, H. Gu, R. Matsumoto, K. Motohashi, Y. Nakayama, K. Zhao and Y. Cui, *Nat. Energy*, 2021, **6**, 790–798.

39 S. Huang, Z. Wu, B. Johannessen, K. Long, P. Qing, P. He, X. Ji, W. Wei, Y. Chen and L. Chen, *Nat. Commun.*, 2023, **14**, 5678.

40 G. Nuroldayeva, D. Adair, Z. Bakenov and B. Uzakbaiuly, *ACS Omega*, 2023, **8**, 37899–37907.

41 F. Schmidt, S. Ehrling, K. Schönherr, S. Dörfler, T. Abendroth, H. Althues and S. Kaskel, *Energy Technol.*, 2021, **10**, 2100721.

42 W. M. Dose, C. Xu, C. P. Grey and M. F. L. De Volder, *Cell Rep. Phys. Sci.*, 2020, **1**, 100253.

43 W. M. Dose, J. K. Morzy, A. Mahadevegowda, C. Ducati, C. P. Grey and M. F. L. De Volder, *J. Mater. Chem. A*, 2021, **9**, 23582–23596.

44 I. Bloom, L. K. Walker, J. K. Basco, D. P. Abraham, J. P. Christophersen and C. D. Ho, *J. Power Sources*, 2010, **195**, 877–882.

45 H. Cha, J. Kim, H. Lee, N. Kim, J. Hwang, J. Sung, M. Yoon, K. Kim and J. Cho, *Adv. Mater.*, 2020, **32**, e2003040.

46 Q. An, Q. Liu, P. Mao, L. Duan, H. Y. Zhu, L. Liu, G. Zhao, Y. Zha, L. Yang, M. Sun, Y. Fan, F. Xie, G. Hu and H. Guo, *Angew. Chem., Int. Ed.*, 2025, e202422539, DOI: **10.1002/anie.202422539**.

47 H. H. Ryu, N. Y. Park, D. R. Yoon, U. H. Kim, C. S. Yoon and Y. K. Sun, *Adv. Energy Mater.*, 2020, **10**, 2000495.

48 H. Oh, G.-S. Kim, J. Bang, S. Kim and K.-M. Jeong, *Energy Environ. Sci.*, 2025, **18**, 645–658.

49 Z. Qu, Y. Wang, C. Zhang, S. Geng, Q. Xu, S. Wang, X. Zhao, X. Zhang, B. Yuan, Z. Ouyang and H. Sun, *Adv. Mater.*, 2025, **37**, e2410974.

50 Z. Wei, D. Kong, L. Quan, J. He, J. Liu, Z. Tang, S. Chen, Q. Cai, R. Zhang, H. Liu, K. Xu, L. Xing and W. Li, *Joule*, 2024, **8**, 1350–1363.

51 M. Ryu, Y. K. Hong, S. Y. Lee and J. H. Park, *Nat. Commun.*, 2023, **14**, 1316.

52 H. Sul, D. Lee and A. Manthiram, *Small*, 2024, **20**, e2400728.

53 J. A. Barreras-Uruchurtu, N. Besnard, C. Paul, L. Marchal, S. Devisme and B. Lestriez, *J. Electrochem. Soc.*, 2025, **172**, 020522.

54 S. Han, E.-H. Noh, S. Chae, K. Kwon, J. Lee, J.-S. Woo, S. Park, J. W. Lee, P. J. Kim, T. Song, W.-J. Kwak and J. Choi, *J Energy Storage*, 2024, **96**, 112693.

55 Y. Liu, X. Gong, C. Podder, F. Wang, Z. Li, J. Liu, J. Fu, X. Ma, P. Vanaphuti, R. Wang, A. Hitt, Y. Savsatli, Z. Yang, M. Ge, W.-K. Lee, B. Yonemoto, M. Tang, H. Pan and Y. Wang, *Joule*, 2023, **7**, 952–970.

56 Y. Zhang, S. Lu, F. Lou and Z. Yu, *Energy Technol.*, 2022, **10**, 2200732.

57 G. Oltean, N. Plylahan, C. Ihrfors, W. Wei, C. Xu, K. Edström, L. Nyholm, P. Johansson and T. Gustafsson, *Batteries*, 2018, **4**, 2.

58 U. Pal, B. Roy, M. Hasanpoor, H. Ilbeygi, T. Mendes, R. Kerr, L. Vazhapully, C. Song, D. Wang, M. Boot-Handford, M. G. Sceats, M. Forsyth, D. Al-Masri and P. C. Howlett, *Batteries Supercaps*, 2024, **7**, e202400072.

This journal is © The Royal Society of Chemistry 2025

Energy Environ. Sci., 2025, **18**, 8446–8461 | **8461**